Flapping-mode changes and aerodynamic mechanisms in miniature insects

Yu Zhu Lyu, Hao Jie Zhu, and Mao Sun[*]

Institute of Fluid Mechanics, Beihang University, Beijing 100191, China

Miniature insects fly at very low Reynolds number (Re); low Re means large viscous effect. If flapping as larger insects, sufficient vertical force cannot be produced. We measure the wing kinematics for miniature-insect species of different sizes and compute the aerodynamic forces. The planar upstroke commonly used by larger insects changes to a U-shaped upstroke, which becomes deeper as size or Re decreases. For relatively large miniature insects, the U-shaped upstroke produces a larger vertical force than a planar upstroke by having a larger wing velocity and, for very small ones, the deep U-shaped upstroke produces a large transient drag directed upwards, providing the required vertical force.

I. INTRODUCTION

Approximately half of the existing winged-insect species are of small size [1] (wing length $R \approx 0.5$–4 mm; referred to as miniature insects). But much of what we know about the biomechanical mechanisms of insect flight is derived from studies on medium and large insects ($R \approx 5$–50 mm), such as flies, honey bees, and hawkmoths [2–11]. The nondimensional parameter representing the effect of air viscosity is the Reynolds number (Re): lower Re means the wing moves in a more viscous flow. In the present paper, Re is defined as Re $= cU/\nu$, where c is the mean chord length of the wing, U is the mean wing speed at the radius of gyration of the wing (r_2), and ν is the kinematic viscosity of the air (U is defined as $U = 2\Phi f r_2$, where Φ is the stroke aptitude and f is the stroke frequency). For the flapping wing of an insect, Re is approximately proportional to $R^{1.33}$ [1]. Thus, the wings of miniature insects operate at very low Re, of the order of 80–10. At this range of Re, moving in the air is like moving in mineral oil.

Medium and large insects in normal hovering beat their wings back and forth in an approximately horizontal plane called upstroke and downstroke, respectively [12–15] (Fig. 1). In the present paper, when an upstroke (or a downstroke) is approximately in a plane, we call it a planar upstroke (or planar downstroke). The wings operate at Reynolds number (Re) of approximately 100–3500. During the downstroke or upstroke, a lift and a drag that is a little smaller are produced (Fig. 1). The lift provides the weight-supporting vertical force; the drag in the downstroke cancels out that in the upstroke and the flapping-cycle mean horizontal force is zero. The aerodynamic forces are generated mainly by the leading-edge vortex (LEV) that attaches to the wing in the entire up- or downstroke, which is referred to as the delayed-stall mechanism [2–11]. However, if miniature insects flap their wings as their larger counterparts do, sufficient aerodynamic force cannot be produced because of the very strong viscous

effects: the LEV is significantly defused and little lift can be generated, while the drag is very large [16,17]. Miniature insects must use different wing kinematics and aerodynamic mechanisms from those of the medium and large insects.

Recently, we studied the hovering flight of a relatively large miniature insect, the fruitfly *Drosophila virilis* (DV) ($R \approx 3$ mm) [18], and a very small one, the small wasp *Encarsia Formosa* (EF) ($R \approx 0.5$ mm) [19]. Re of the fruitfly is approximately 80 and that of the small wasp is approximately 10 (note that in many literature papers, Re for fruitflies is larger than the above value, between 130–200; this is because, in these papers, a larger reference speed, i.e., wing-tip speed, and a larger reference length, i.e., chord length at $0.7R$, are used). From these two studies, we observe that the wasp has a very deep U-shaped upstroke and the fruitfly also has a U-shaped upstroke but much shallower, and that the deep U-shaped upstroke can generate a large transient drag that pointed almost upwards, enhancing the vertical force production.

Here, based on the above observations, we put forth a hypothesis on how the flapping mode changes: as insect size or Re decreases, a deeper and deeper U-shaped upstroke will be used to overcome the viscous effect. We test this hypothesis by measuring the wing kinematics of more species of different sizes and obtain data for Re ranging from approximately 80 to 10 and by computing the aerodynamic forces. The data and computation support our hypothesis: the planar upstroke changes to a U-shaped upstroke which becomes deeper as size or Re becomes smaller; for relatively large miniature insects, the U-shaped upstroke produces a larger vertical force than a planar upstroke by having a larger wing velocity, and for very small ones, the deep U-shaped upstroke produces a large transient drag that points almost upwards by fast downward acceleration of the wing, providing the required vertical force.

II. MATERIALS AND METHODS

A. Insects

Thrips (FO) were acquired from the Laboratory of Institute of Vegetables and Flowers, Chinese Academy of Agricultural Sciences, which are descendants of wild-caught *Frankliniella*
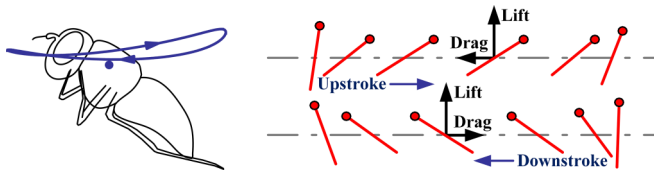
---

*m.sun@buaa.edu.cn

FIG. 1. Left: the wing-tip trajectory (projected onto the symmetrical plane) of a dronefly *Eristalis tenax* (ET) [15], a relatively large insect. Right: the motion of a section of the wing.

occidentalis. Biting midges *Forcipomia gloriose* (FG), *Dasyhelea flaviventris* (DF), and gall midges *Anbremia* sp. (AS) were netted in a suburb of Beijing in June to August 2017.

B. High-speed filming

The near-hover flights of the miniature insects in transparent flight chambers were filmed using three orthogonally aligned synchronized high-speed cameras (FASTCAM Mini UX100, Photron Inc., San Diego, CA) mounted on an optical table [Fig. 2(a)]. The size of the flight chamber is $50 \times 50 \times 50$ mm^3 for biting midge *Forcipomia gloriose* (FG) and $34 \times 34 \times 34$ mm^3 for biting midge *Dasyhelea flaviventris* (DF), gall-midge *Anbremia* sp. (AS), and thrip *Frankliniella occidentalis* (FO). Each camera was equipped with a 60 mm micro-Nikkor lens and 12 mm extension tube. For FG, the cameras were set to 10 000 (or 10 500) frames per second (resolution 1280×496 or 1280×472) pixels and shutter speed to 20 μs; for DF, AS, and FO, the cameras were set to 8000 frames per second (resolution 1280×624 pixels) and shutter

FIG. 3. Video sequences of a gall midge (AS) at hovering; three camera views are shown. Times noted are ms from the instant when the upstroke starts.

speed to 20 μs. Each camera view was backlit using a 50 W integrated red-light emitting diode (LED; luminous flux, 4000 lm; wavelength, 632 nm) and two lenses were used to make the light uniform. The synchronized cameras were manually triggered when the insect was observed to fly steadily in the filming area (approximately $6 \times 6 \times 6$ mm^3), which represented the intersecting field of views of the three cameras. The experiment was performed at temperature 25–27 °C and relative humidity 50–60%.

C. Kinematics reconstruction

The orthogonally aligned cameras were calibrated by using a flat glass panel with a high-accuracy black-and-white checkerboard pattern printed on it. The calibration gave the intrinsic and extrinsic parameters of each camera which determined the transform matrix of the camera [15,20].

The method used to extract the three-dimensional (3D) body and wing kinematics from the filmed data was developed in previous works of our group [15,19,20]. The body and wings were represented by models [Fig. 2(b)]. The model of the body was two lines perpendicular to each other, which were the line connecting the head and the end of the abdomen and the line connecting the two wing hinges [Fig. 2(b)]. The model of a wing was the outline of the wing obtained by scanning the cutoff wing [Fig. 2(d)] and the wing model can have a spanwise bending, represented by the maximum bending displacement [Fig. 2(c)]. From our observation, small insects appear to have larger wing bending than the larger ones. As an example, the wing bending can be clearly seen in the video sequences of a gall midge (AS) shown in Fig. 3. Without taking bending into account, satisfactory match between model wing and filmed wing cannot be achieved. An interactive graphic user interface developed using MATLAB (v.7.1, The Mathworks, Inc., Natick, MA) was used to determine the positions and orientations of the body and the wings: at each time step, the positions and orientations of
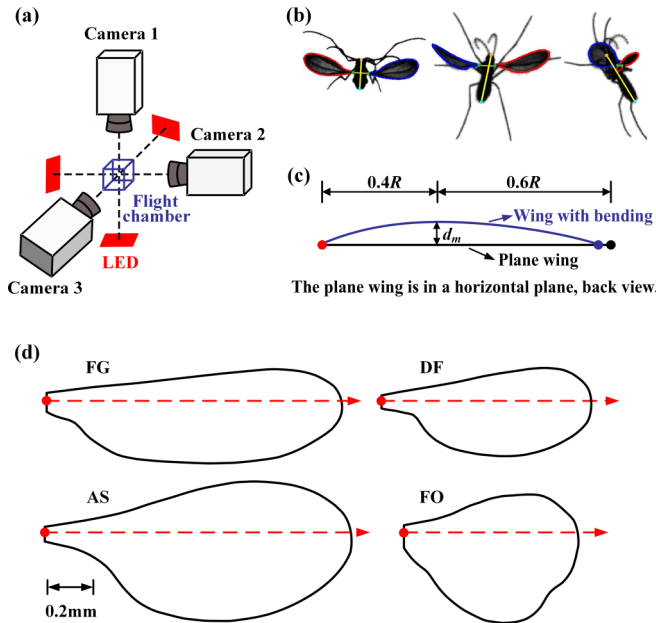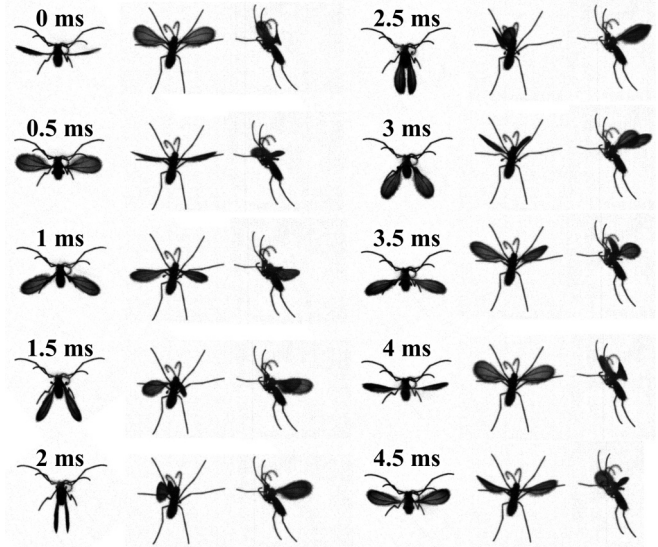

FIG. 2. Experimental setup, kinematics extraction, and wing bending definition. (a) A sketch showing the flight chamber and cameras. Each camera view is backlit using an integrated red-light emitting diode (LED). (b) Extraction of body and wing kinematics. (c) Definition of the spanwise bending of the wing. d_m: maximum bending displacement, assumed to be at $0.4R$. (d) Planforms, or wing outlines.

the models of the body and wings were adjusted until the best overlap between a model image and the displayed frame was achieved in three views, and at this point the positions and orientations of these models were taken as the positions and orientations of the body and the wings. At a time step, the model wing is first set as a plane wing without bending. If the filmed wing does not have bending, the position and orientation of the plane model wing can be adjusted to match the filmed wing. When there is bending in the filmed wing, the maximum bending displacement [d_m, Fig. 2(c)] is also adjusted in the process. The fitting process was manually done. A more detailed description of the method can be found elsewhere [15,19,20].

This process gives the position and orientation of the body, the wing root positions, the Euler angles, and the maximum bending displacement of the wings. We processed 360 wingbeats in total, with over 20 flight sequences from 20 individuals: 30 wingbeats for each of the five biting midges *Forcipomia gloriose* and for each of the five biting midges *Dasyhelea flaviventris* (these two species have high wingbeat frequency); and six wingbeats for each of the five gall midges *Anbremia* sp. and for each of the five thrips *Frankliniella occidentalis*.

D. Flow calculation

The flows around and the aerodynamic force acting on the insects were computed using the method of computational fluid dynamics (CFD). For medium and large insects at hovering flight, it had been shown that the aerodynamic interaction between the body and the wings was negligibly small: the aerodynamic force in the case with body-wing interaction was less than 2.5% different from that without body-wing interaction [21]. Our computations showed that this also true for the miniature insects. Therefore, in the present CFD model, only the two wings were considered. The planform of a model wing is approximately the same as that of the corresponding insect wing. The wing planforms for FG, DF, AS, and FO are shown in Fig. 2(d) and those for ET, DV, LS, and EF can be found in our previous works [15,18,19,22]. The section of the model wing is a flat plat of 3% thickness with rounded leading and trailing edges.

The governing equations of the flow are the incompressible Navier-Stokes equations. They have the following dimensionless form:

$$\nabla \mathbf{u} = 0, \tag{1}$$

$$\frac{\partial \mathbf{u}}{\partial t} + \mathbf{u}\nabla \mathbf{u} = -\nabla p + \left(\frac{1}{\text{Re}}\right)\nabla^2 \mathbf{u}, \tag{2}$$

where $\mathbf{u}$ is the nondimensional fluid velocity field, t is the nondimensional time, p is the nondimensional fluid pressure, Re is the Reynolds number, ∇ is the gradient operator, and ∇^2 is the Laplacian operator; in the nondimensionalization, U, c, and c/U are taken as reference velocity, length, and time, respectively (here, U is the mean flapping velocity at the radius of the second moment of wing area and c is the mean chord length of the wing). The Navier-Stokes equations were solved over moving overset grids because there are
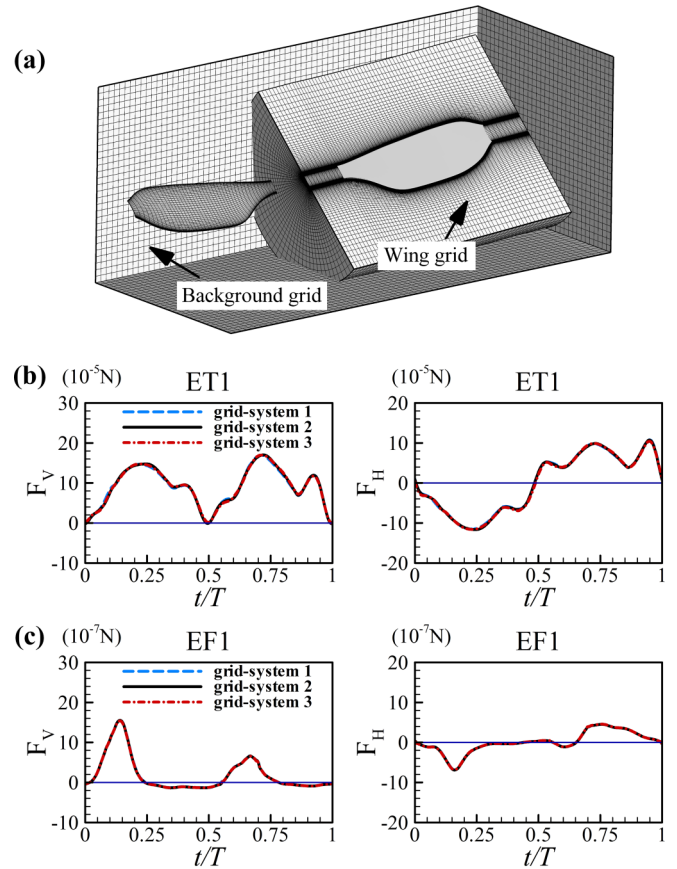

FIG. 4. (a) Portions of a computational grid system. (b),(c) Time courses of the vertical and horizontal forces in one cycle, calculated with three grid systems, for ET1 and EF1, respectively.

relative movements between the left and right wings. There was a body-fitted curvilinear grid for each of the wings and a background Cartesian grid which extends to the far-field boundary of the domain [Fig. 4(a)]. The body-fitted wing grid is regenerated at each time step during the computation because of the spanwise bending of the wings. The flow solver, which was based on an artificial compressibility method developed by Rogers *et al.* [23], was the same as that used in several previous studies of our group [6,19,24]; its detailed description can be found there.

The solver has been validated by comprehensive tests [19]: comparison has been made with the measured data of a revolving wing (Re = 500) [25] and a flapping wing (Re = 180) [26]; and comparison has been made with theoretical (Stokes and Oseen solutions) and measured results for a sphere at very low Re (5–20) [27].

Grid resolution tests were conducted to ensure that the flow calculations were grid independent. For the dronefly (ET) wing (Re = 720), three grid systems were considered. For grid system 1, the wing grid had dimensions $41 \times 61 \times 43$ in the normal direction, around the wing, and in the spanwise direction, respectively (first layer grid thickness was $0.0015c$); the background grid had dimensions $81 \times 81 \times 81$ in the X, Y, and Z directions, respectively. For grid system 2, the corresponding grid dimensions were $65 \times 91 \times 65$ and $121 \times 121 \times 121$ ($0.001c$). For grid system 3, the corresponding
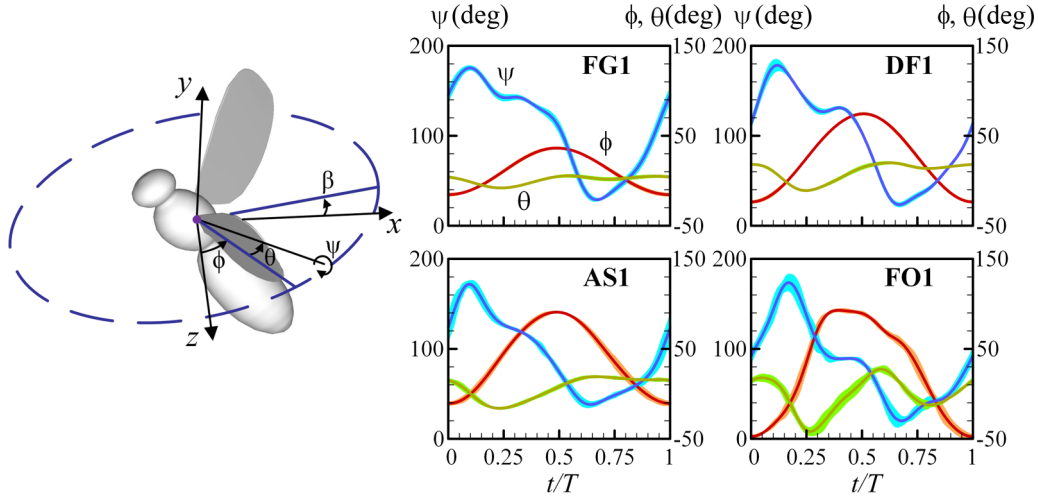
FIG. 5. Left: reference frame and Euler angles defining the wing kinematics: (x, y, z) are coordinates in a system with its origin at the wing root and with x-axis points horizontally backwards, y-axis points vertically upwards, and z-axis points to the left of the insect. ϕ is the positional angle (in the stroke plane), ψ is the pitch angle, θ is the deviation angle, and β is the stroke-plane angle. Right: measured Euler angles of biting midge FG1 (mean $\pm$ s.d.; $n = 30$ wingbeats), biting midge DF1 (mean $\pm$ s.d.; $n = 30$ wingbeats), gall midge AS1 (mean $\pm$ s.d.; $n = 6$ wingbeats), and thrip FO1 (mean $\pm$ s.d.; $n = 6$ wingbeats). T: stroke period.

grid dimensions were $91 \times 135 \times 96$ and $181 \times 181 \times 181$ ($0.00067c$). For all three grid systems, grid points of the background grid concentrated in the near field of the wings where its grid density was approximately the same as that of the outer part of the body grid. Three grid systems similar to the above were also used for the small wasp (EF) wing (Re = 10). The aerodynamic forces computed are shown in Figs. 4(b) and 4(c). It is seen that there is almost no difference between the force coefficients calculated by the three grid systems. Calculations were also conducted using a larger computational domain. The domain was enlarged by adding more grid points to the outside of the background grid of grid system 2. The calculated results showed that there was no need to put the outer boundary further than that of grid system 2. The above results showed that grid system 2 was proper for the wings of ET and EF. The wings of fruitfly DV, biting midge DF, and gall midge AS had similar aspect ratio as that of ET or EF and operated at Re between those of ET and EF; therefore, grid system 2 was also used for insects of these four species. For biting midge FG, whose wing had a much larger aspect ratio, the wing grid in grid system 2 was changed to $65 \times 91 \times 70$ (more points in the spanwise direction); and for thrip FO, whose wing had a smaller aspect ratio, the wing grid was changed to $65 \times 91 \times 56$ (less points in the spanwise direction). The effect of the time-step value was also studied and it was found that a numerical solution effectively independent of the time step was achieved if the time-step value was $\leqslant T/440$, and this value was used in all the calculations.

III. RESULTS AND DISCUSSION

A. Wing kinematics

We use high-speed cameras equipped with microlenses and extension tubes to film the approximately hovering flight of the miniature insects and extract the wing kinematics using an interactive graphic user interface. A few years earlier, we

measured the wing motion of vegetable leafminers *Liriomyza sativae* (LS) ($R \approx 1.5$ mm and Re ≈ 40) [22]. Here, the wing kinematics of four more species is measured: biting midges *Forcipomia gloriose* (FG) and *Dasyhelea flaviventris* (DF), gall midge *Anbremia* sp. (AS), and thrip *Frankliniella occidentalis* (FO). Their Re is 30, 24, 17, and 14, respectively, and is between those of LS (40) and EF (10).

If the wing is a plane wing without bending, its orientation can be determined by the Euler angles (see the left subplot in Fig. 5). When the wing has bending, the bending (represented by the maximum bending displacement d_m) is superposed to the plane wing, and the Euler angles of the bending wing are those of the corresponding plane wing. Figure 5 shows the measured Euler angles of the wing in four individuals, each from one of the four species; the corresponding bending displacement is given in the Appendix (Fig. 11). The original video sequences for the insects are presented as supplemental movies 1–4 (see Supplemental Material [28]). For each of the four species, data of another four individuals were also measured (Fig. 11 and Table I in the Appendix); within a species, the results are similar (see Fig. 11 in the Appendix).

Using the data in Fig. 5, stroke diagrams showing the flapping mode of the four insects are plotted in Fig. 6 (those of the miniature insects DV [18], LS [22], and EF [20] are also included); for comparison, the stroke diagram of a large insect, the dronefly *Eristalis tenax* (ET) [15], is also plotted in the figure. The following is observed. The large insect ET [Fig. 6(a)] has approximately planar upstroke and downstroke, while for the miniature insects [Figs. 6(b)–6(h)], the upstroke changes to a U shape. As size or Re decreases, the U-shaped upstroke becomes deeper and deeper [Figs. 6(b)–6(h)]. For the two very small insects, thrip FO and wasp EF, the downstroke is also U shaped, which is the result of the "fling" motion discovered by Weis-Fogh [12] and described in detail in [19,24,29–31]; but the downstroke U-shaped curve is much shallower than that of the upstroke of the insect [Figs. 6(g) and 6(h)]. Within each of the species, all the
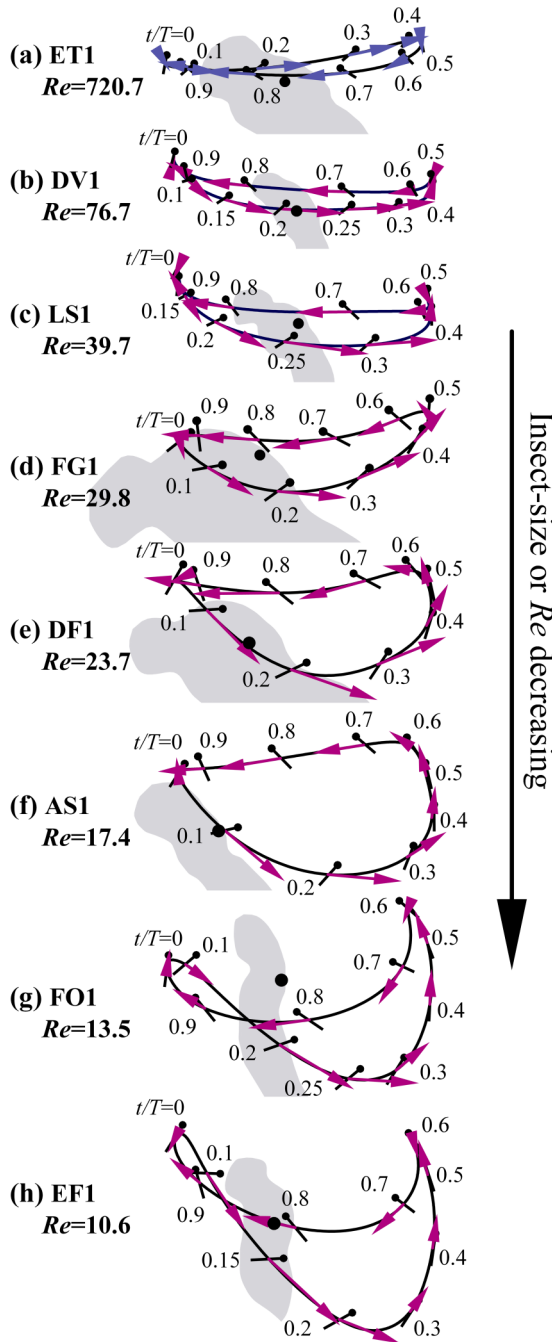
FIG. 6. Stroke diagrams show the wing motions of the insects. The solid curve indicates the wing-tip trajectory (projected onto the $x-y$ plane); black lines indicate the orientation of the wing at various times in one stroke cycle, with dots marking the leading edge; a black dot defines the wing-root location on the insect body; the purple arrow represents the velocity of the wing at the radius of gyration.

individuals have the same flapping pattern (see Fig. 12 in the Appendix).

Figure 6 also shows the orientation and velocity of the wing at various times of the stroke cycle (here, the wing section and velocity at the radius of gyration of the wing are used to represent the wing and its velocity, respectively). It is seen [Figs. 6(b)–6(h)] that in the early part of the U-shaped upstroke ($t/T \approx 0$–0.2), the wing accelerates downwards and
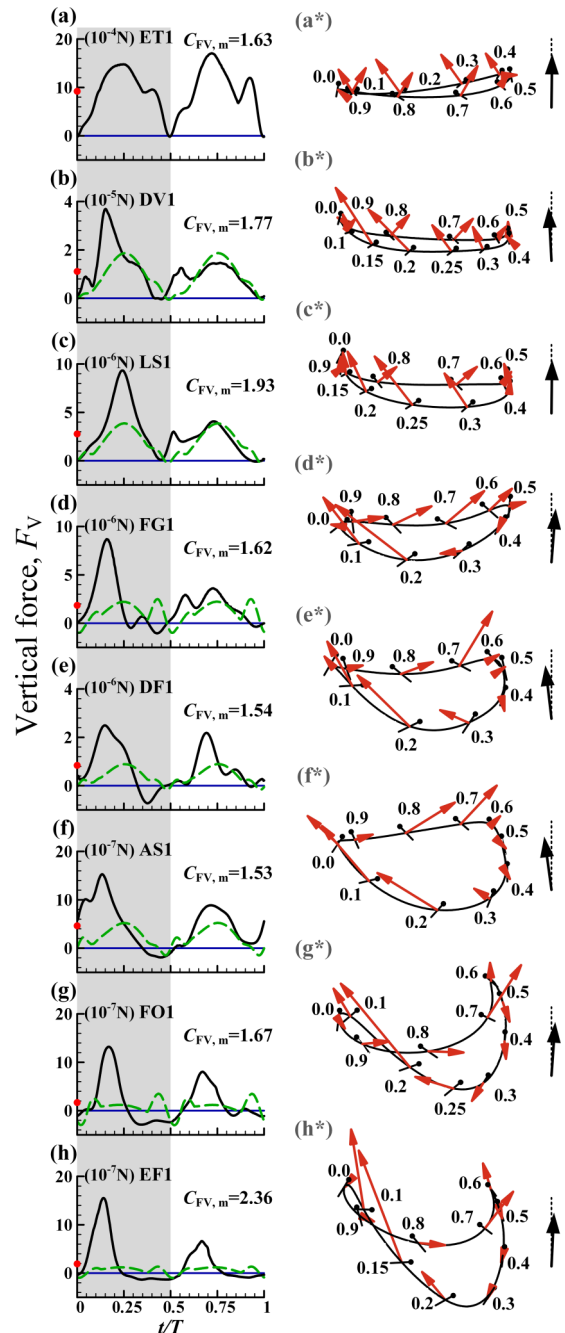
FIG. 7. (a)–(h) Vertical force (F_V) in one stroke cycle (black line); $C_{FV,m}$ is the stroke-cycle mean vertical force coefficient (defined as the mean of F_V divided by $0.5\rho U^2 2S$, where S is the wing area and U is the mean wing speed at the radius of gyration of wing); the red dot on the vertical axis represents the estimated weight of the insect. In (b)–(h), the green dashed line represents the vertical force produced if the upstroke was assumed planar. (a*)–(h*) Instantaneous force vectors superimposed on a diagram of wing motion. The large black vector to the right of each set of traces indicates the orientation of the stroke-cycle mean force vector.

backwards with the wing surface almost horizontally and at a rather large angle of attack; the smaller the insect or the lower the Re, the larger the acceleration [see the change in wing speed in Figs. 6(b)–6(h)]. In the later part of the U-shaped
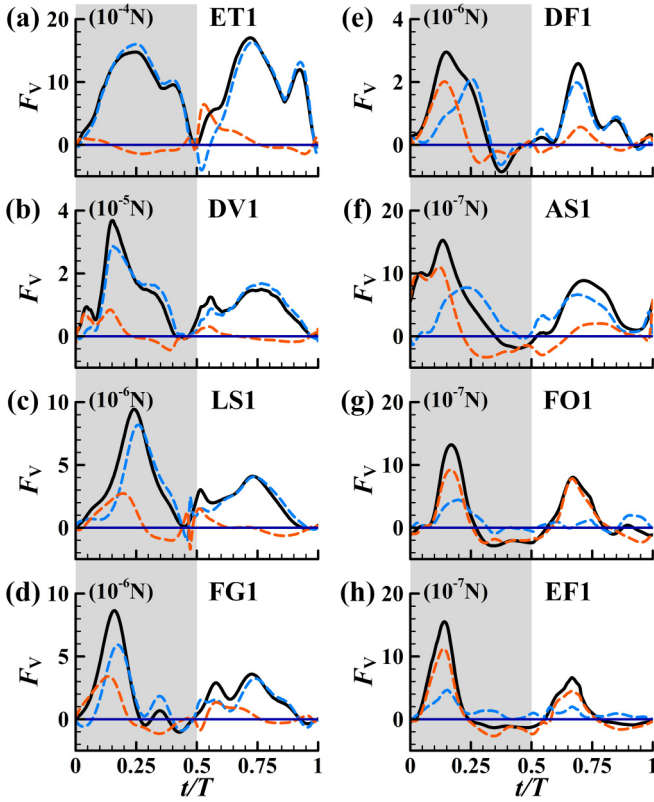
FIG. 8. Vertical force in one stroke cycle (black line); contribution by the lift (blue line) and that by the drag (orange line); gray background indicates the upstroke.
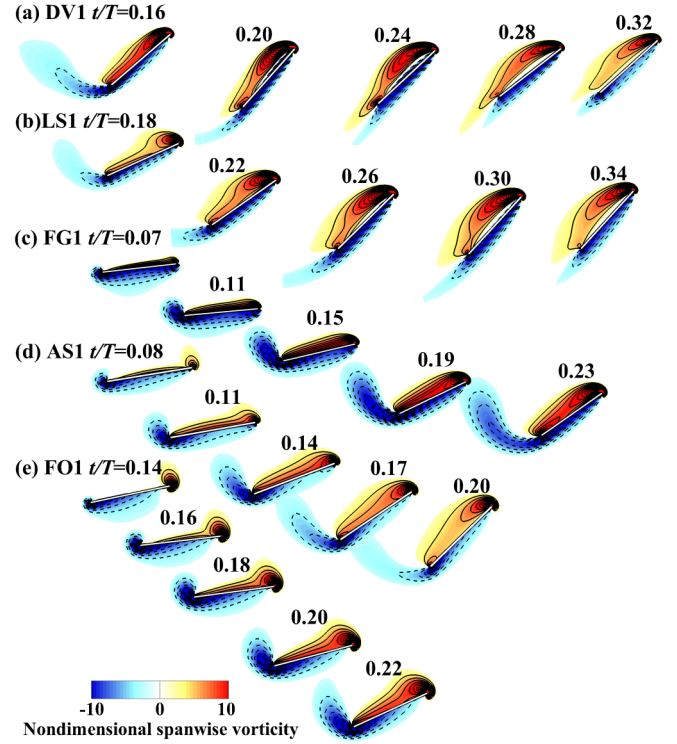

FIG. 9. Nondimensional spanwise vorticity contours in the section at the radius of gyration, at various times during the U-shaped upstroke. Vorticity is nondimensionalized by U/c, where c is the mean chord length of the wing; solid and dashed lines denote the anticlockwise and clockwise vorticity, respectively. The magnitude of the nondimensional vorticity at the outer contour is 4 and the contour interval is 2.

upstroke, in general, the wing moves slower [Figs. 6(e)–6(h)]; and as Re becomes very small, the wing moves almost vertically upwards with the wing surface vertical and the angle of attack close to zero [Figs. 6(e)–6(h)]. It is expected that the first part of the novel upstroke, in which the wing smashes on the air, will generate a large drag directing upwards (vertical force), whereas the second part of the upstroke, in which the wing slices through the air, generates smaller drag.

B. Aerodynamic forces

To assess how the weight-supporting vertical force is generated, the flow and forces on the wings were computed using a well-tested flow solver. The computed vertical forces (F_V) are given in Figs. 7(a)–7(h) for the eight insects shown in Figs. 6(a)–6(h) (the corresponding horizontal forces are given in Fig. 13 in the Appendix; the computed vertical and horizontal forces for the other individuals of each species are given in Fig. 14 in the Appendix).

It is seen that for the large insect ET [Fig. 7(a)], the F_V in the upstroke ($t/T = 0$–0.5) is similar to that in the downstroke ($t/T = 0.5$–1); but for the miniature insects [Figs. 7(b)–7(h)], the U-shaped upstroke produces a large F_V peak, while the planar downstroke produces a relatively small F_V. In general, as size or Re decreases, the F_V peak in the U-shaped upstroke becomes higher and narrower [for the two very small insects, FO and EF, a smaller F_V peak is also produced at the early downstroke by the aforementioned fling motion; Figs. 7(g) and 7(h), $t/T = 0.55$–0.7].

To show the advantage of having a U-shaped upstroke for the miniature insects, we made test calculations in which both the down- and upstrokes were planar and horizontal, like those of the larger insects, while Re was kept the same. The computed vertical forces for the seven miniature insects are also shown in Figs. 7(b)–7(h) (the corresponding horizontal forces are given in Fig. 13 in the Appendix). It is seen that the planar upstroke produces much less vertical force than the U-shaped upstroke and it is more so as Re becomes smaller. For the fruitfly DV (Re ≈ 77), the mean vertical force produced by the U-shaped upstroke is 1.43 times that by the planar upstroke. For LS (Re ≈ 40), FG (Re ≈ 30), DF (Re ≈ 24), AS (Re ≈ 17), FO (Re ≈ 14), and EF (Re ≈ 10), the corresponding numbers are 1.82, 1.75, 1.92, 2.27, 2.27, and 4.17, respectively. We thus see that the U-shaped upstroke can produce a large vertical force at very small Reynolds number condition.

The horizontal force (F_H) of each insect (Fig. 13 in the Appendix) is negative (forward pointing) in the upstroke and positive (backward pointing) in the downstroke. Since the insects are in approximately hovering flight, the stroke-cycle mean horizontal force should be zero, or the mean force vector should be in the vertical direction. As can be seen in Figs. 7(a*)–7(h*), the angle between the mean total force and the vertical is no more than 8°, i.e., the mean force vector is very close to being vertical.
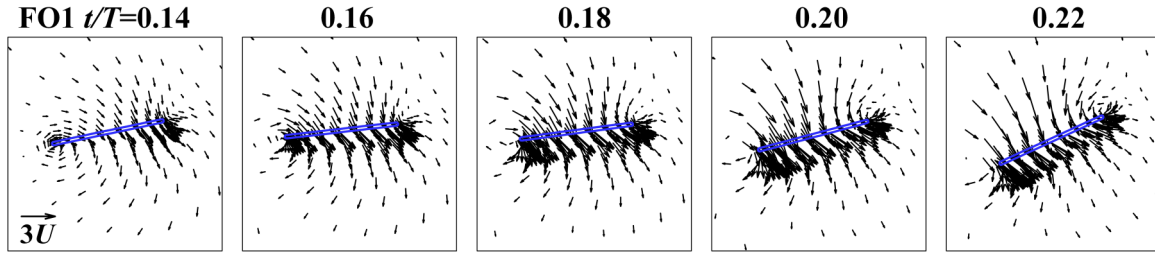
FIG. 10. Nondimensional velocity vector plot in the section at the radius of gyration, at various times during the U-shaped upstroke of FO1, whose vorticity contour plots are shown in Fig. 9(e).

C. Discussion

The above results support our hypothesis: for miniature insects, the planar upstroke changes to U-shaped upstroke and, as insect size or Re decreases, a deeper and deeper U-shaped upstroke will be used to overcome the viscous effect.

The vertical and horizontal forces of a wing come from its lift and drag, which are the components of the total aerodynamic force that are perpendicular and parallel to the wing velocity, respectively. The contributions of the lift and the drag of the wing to the vertical force are plotted in Figs. 8(a)–8(h) (the corresponding contributions to the horizontal force are given in Fig. 15 in the Appendix). For the large insect ET [Fig. 8(a)], almost all the vertical force is contributed by the lift. For the relatively large miniature insects DV and LS [Figs. 8(b) and 8(c)], vertical force is mainly (approximately 90%) contributed by the lift. As insects become smaller [Figs. 8(d)–8(h)], the drag has more and more contribution;

for the two smallest insects, FO and EF, approximately 70% of the vertical force is from the drag.

To explain the large force in the U-shaped upstroke, vorticity fields are plotted for the period in which the large aerodynamic force is produced. We first consider DV and LS, whose size is relatively large and Re is relatively high (approximately 80–40). Figure 9(b) shows the vorticity plots of LS1 in the period of $t/T = 0.18$–0.34: the LEV attaches and moves with the wing, indicating that the force is produced by the delayed-stall mechanism. It can be shown that the planar downstroke also uses the delayed-stall mechanism to produce the force. The reason for the U-shaped upstroke producing a larger force than the planar downstroke is that it has a larger wing velocity [see Fig. 6(c)]. The forces of DV can be similarly explained.

Next we consider the smaller insects [Figs. 9(c)–9(e)]. From vorticity dynamics theory, the aerodynamic force on a

TABLE I. Flight parameters.

ID	Re	R (mm)	S (mm^2)	r_2/R	l_r (mm)	l_b (mm)	f (Hz)	Φ (deg)	β (deg)	u (m/s)	w (m/s)	$F_{V,m}$ (μN)	η (deg)
FG1	29.8	1.30	0.38	0.60	0.53	2.29	1117	52	5.3	0.00	0.00	1.849	4.5
FG2	35.9	1.40	0.44	0.60	0.57	2.36	1112	55	2.6	0.02	0.14	2.350	1.3
FG3	34.8	1.40	0.46	0.60	0.59	2.47	1019	55	−4.1	0.10	0.21	2.622	− 1.4
FG4	31.9	1.34	0.41	0.60	0.55	2.33	1107	52	7.2	0.12	0.07	2.216	0.9
FG5	29.3	1.38	0.45	0.59	0.58	2.40	1016	49	12.6	0.00	0.00	1.679	− 8.6
DF1	23.7	0.92	0.25	0.60	0.27	1.34	723	98	0.9	0.01	0.01	0.840	− 6.6
DF2	23.9	0.95	0.22	0.63	0.28	1.21	781	97	− 0.2	0.00	0.14	1.056	− 3.3
DF3	19.2	0.88	0.20	0.62	0.25	1.16	724	96	7.7	0.00	0.00	0.690	− 6.5
DF4	20.7	0.84	0.20	0.61	0.28	1.14	739	103	7.8	0.05	0.02	0.690	− 7.0
DF5	21.0	0.92	0.23	0.62	0.29	1.28	698	96	5.8	0.16	0.05	0.717	− 4.4
AS1	17.4	1.33	0.51	0.63	0.25	1.30	238	102	4.8	0.14	0.08	0.463	− 7.7
AS2	14.9	1.28	0.43	0.64	0.20	1.05	230	106	1.3	0.09	0.12	0.340	− 9.5
AS3	18.8	1.36	0.57	0.63	0.25	1.12	230	103	1.9	0.10	0.09	0.481	− 9.3
AS4	20.7	1.47	0.65	0.62	0.31	1.38	226	102	− 3.4	0.11	0.04	0.724	− 3.5
AS5	17.3	1.39	0.54	0.63	0.27	1.22	213	108	− 1.2	0.16	0.03	0.634	− 7.6
FO1	13.5	0.76	0.30	0.59	0.28	1.13	239	140	6.3	0.13	0.17	0.167	4.0
FO2	11.9	0.79	0.29	0.59	0.27	1.23	223	137	18.3	0.22	0.00	0.232	2.6
FO3	13.4	0.83	0.33	0.59	0.26	1.09	213	143	9.9	0.12	0.08	0.223	0.9
FO4	12.6	0.79	0.31	0.57	0.26	1.18	225	141	− 4.4	0.14	0.07	0.205	14.9
FO5	14.3	0.86	0.34	0.61	0.29	1.27	231	134	14.7	0.22	0.11	0.206	0.4

Re: Reynolds number; R: wing length; S: area of wing; r_2: radius of gyration of wing; l_r: the distance between the left and right wing roots; l_b: body length. f and Φ: stroke frequency and amplitude, respectively; β: stroke plane angle; u and w: horizontal and vertical velocities of the body, respectively; $F_{V,m}$: mean vertical force; η: angle from the vertical of the mean force vector.
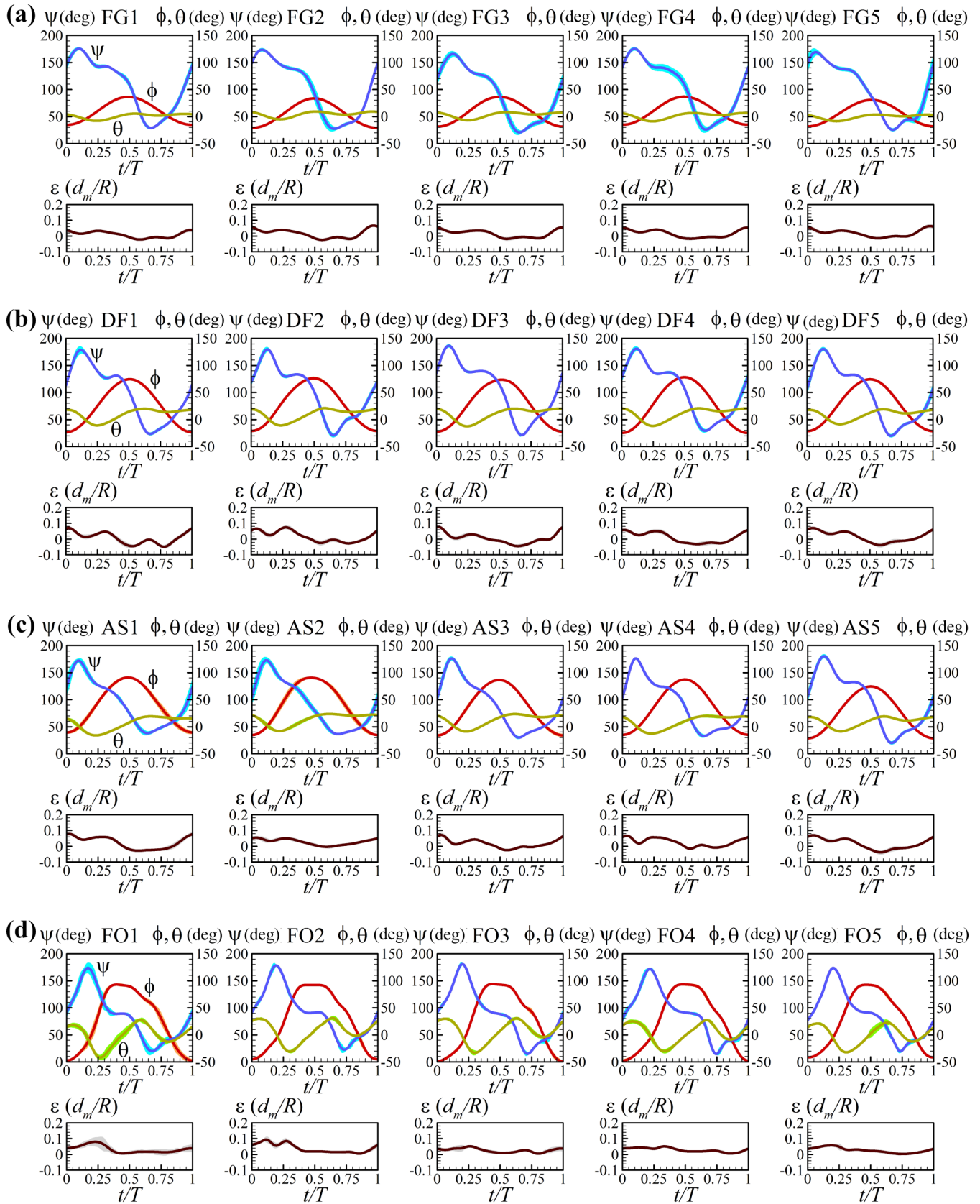
FIG. 11. Wing kinematics for each of the individuals. Measured Euler angles of wing and the maximum spanwise bending displacement ε (d_m/R) in one stroke cycle. (a) Biting midge *Forcipomia gloriose* (FG). (b) Biting midge *Dasyhelea flaviventris* (DF). (c) Gall midge *Anbremia* sp. (AS). (d) Thrip *Frankliniella occidentalis* (FO).
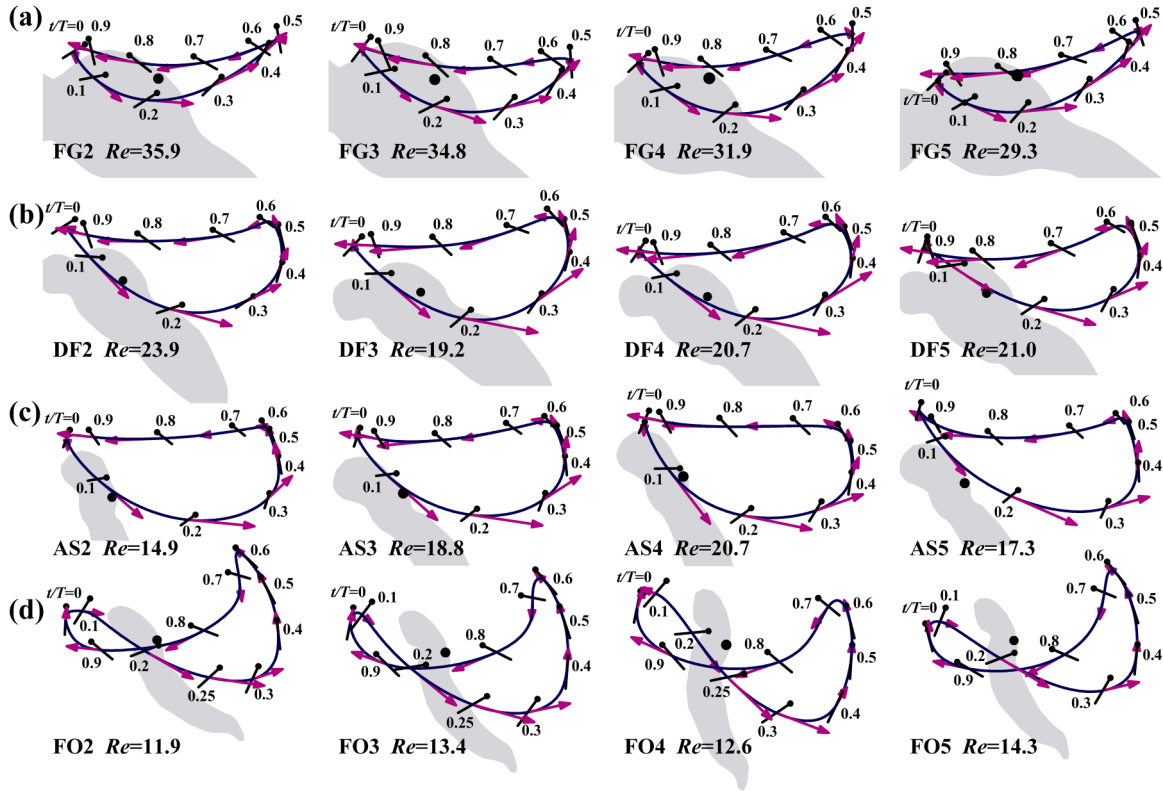
FIG. 12. Stroke diagrams show the wing motions of the insects. (a)–(d) Biting midge FG, biting midge DF, gall midge AS, and thrip FO. The solid curve indicates the wing-tip trajectory (projected onto the x-y plane); black lines indicate the orientation of the wing at various times in one stroke cycle, with dots marking the leading edge; the black dot defines the wing-root location on the insect body; the purple arrow defines the velocity of the wing at the radius of gyration. (Similar plots can be obtained for ET [15], DV [18], LS [20], and EF [19].)

body moving in incompressible fluid is equal to the time rate of change in the first moment of vorticity [32]. When there is some counterclockwise vorticity at the leading edge and some clockwise vorticity at the trailing edge, there will be a first moment of vorticity (just like two opposite forces with a distance in between will give a couple or moment). If the opposite vorticities at the leading and trailing edges grow with time, a time rate of change in the first moment of vorticity, i.e., aerodynamic force, will be produced. As an example, we

look at the vorticity plots of FO [Fig. 9(e)]: during the very short period ($t/T = 0.14$–0.22), counterclockwise vorticity is continuously produced around the leading edge of the wing and clockwise vorticity around the trailing edge. This would give a large time rate of change in the first moment of vorticity, giving the large aerodynamic force. A simple physical explanation of the force can also be given as follows. Figure 10 shows the velocity vectors in a vertical plane at the same section as that in Fig. 9(e) at the corresponding
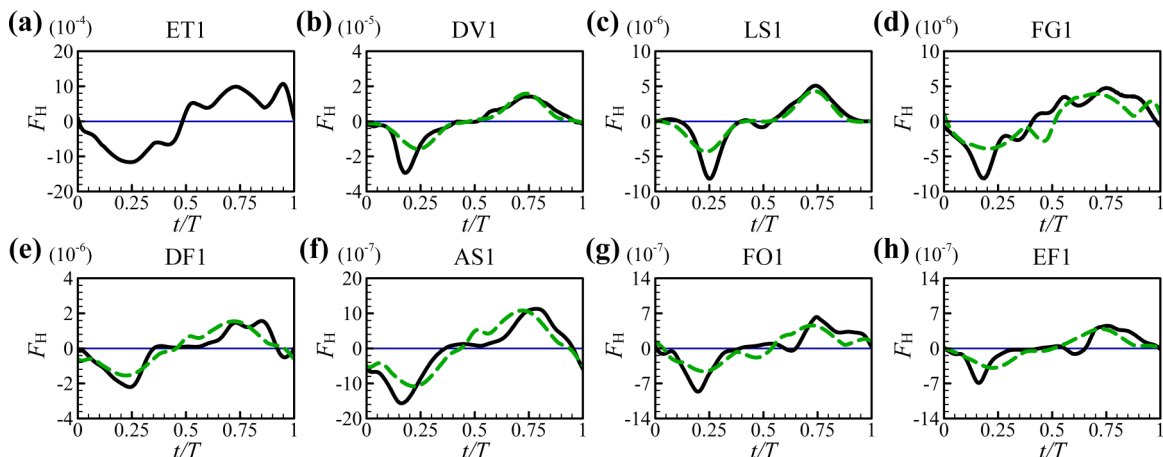

FIG. 13. Horizontal forces (black line) for the eight insects shown in Figs. 2(a)–2(h); in (b)–(h), the green dashed line represents the horizontal force produced if the upstroke was assumed planar.
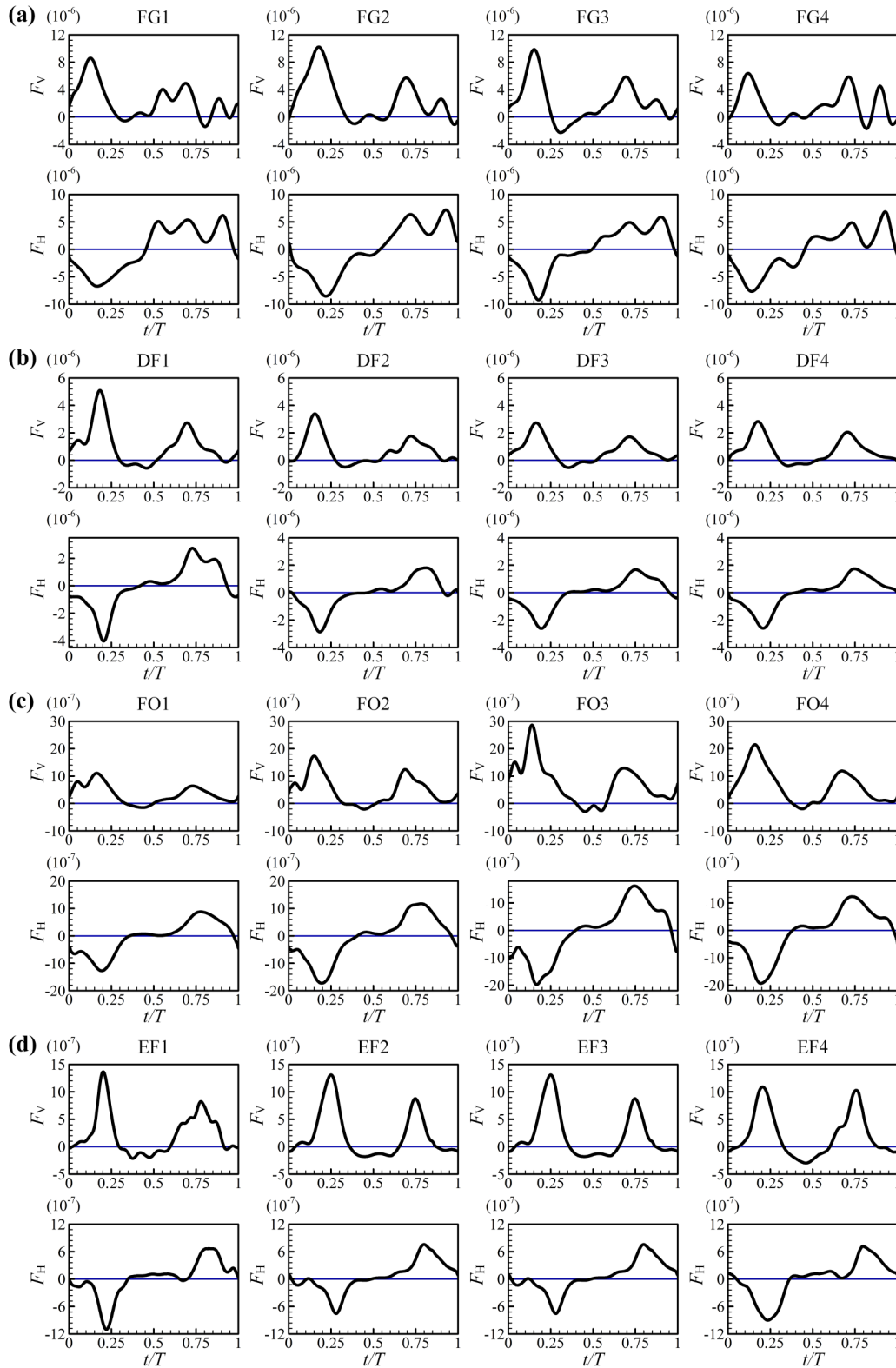
FIG. 14. Vertical and horizontal forces for the other four individuals of each species.

times. It is seen that a large-speed, almost downward jet is induced by the leading-edge and trailing-edge vortices. The jet contains momentum and the momentum is produced in a very short time ($t/T = 0.14$–0.22), and hence a large force

is generated. The above force producing mechanism is called "rowing mechanism" [19,33]: the wing accelerates fast from zero velocity at a very high angle of attack, producing a large transient drag (here, the drag points almost upwards, giving
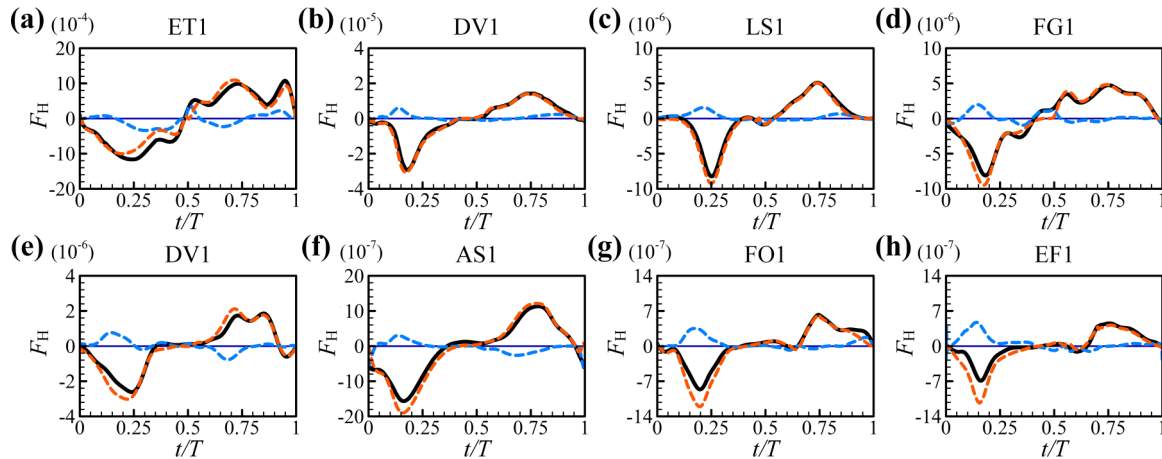
FIG. 15. Horizontal force in one stroke cycle (black line); contribution by the lift (blue line) and that by the drag (orange line).

the large vertical force). The same is true for FG, DF, AS, and EF.

IV. CONCLUSIONS

Miniature insects change their flapping mode to solve the low-Re problem: The planar upstroke changes to a U-shaped upstroke and, as size or Re becomes smaller, a deeper U-shaped upstroke is employed. For relatively large miniature insects (Re approximately 80–40), the U-shaped upstroke produces a larger vertical force than a planar upstroke by having a larger wing velocity, and for very small ones (Re below approximately 40), the deep U-shaped upstroke produces a large transient drag that points almost upwards by fast downward acceleration of the wing, providing the required vertical force. The smaller the insect, the more it relies on drag principle for generation of the weight-supporting vertical force.

APPENDIX

Measured wing kinematics (Figs. 11 and 12), computed forces (Figs. 13–15), and flight parameters (Table I) are shown for all five individuals in each of the four species.

[1] R. Dudley, *The Biomechanics of Insect Flight: Form, Function, Evolution* (Princeton University Press, Princeton, 2002).

[2] C. P. Ellington, C. Van den Berg, A. P. Willmott, and A. L. R. Thomas, Leading-edge vortices in insect flight, Nature (London) **384**, 626 (1996).

[3] M. H. Dickinson, F. O. Lehmann, and S. P. Sane, Wing rotation and the aerodynamic basis of insect flight, Science **284**, 1954 (1999).

[4] H. Liu, C. P. Ellington, K. Kawachi, C. V. D. Berg, and A. P. Willmott, A computational fluid dynamic study of hawkmoth hovering, J. Exp. Biol. **201**, 461 (1998).

[5] R. J. Bomphrey, R. B. Srygley, G. K. Taylor, and A. L. R. Thomas, Visualizing the flow around insect wings, Phys. Fluids **14**, S4 (2002).

[6] M. Sun and J. Tang, Unsteady aerodynamic force generation by a model fruit fly wing in flapping motion, J. Exp. Biol. **205**, 55 (2002).

[7] S. P. Sane, The aerodynamics of insect flight, J. Exp. Biol. **206**, 4191 (2003).

[8] Z. J. Wang, Dissecting insect flight, Ann. Rev. Fluid Mech. **37**, 183 (2005).

[9] D. D. Chin and D. Lentink, Flapping wing aerodynamics: From insects to vertebrates, J. Exp. Biol. **219**, 920 (2016).

[10] J. Lee, H. Choi, and H.-Y. Kim, A scaling law for the lift of hovering insects, J. Fluid Mech. **782**, 479 (2015).

[11] G. Liu, H. Dong, and C. Li, Vortex dynamics and new lift enhancement mechanism of wing-body interaction in insect forward flight, J. Fluid Mech. **795**, 634 (2016).

[12] T. Weis-Fogh, Quick estimates of flight fitness in hovering animals, including novel mechanisms for lift production, J. Exp. Biol. **59**, 169 (1973).

[13] C. P. Ellington, The aerodynamics of hovering insect flight. III. Kinematics, Phil. Trans. R. Soc. London B **305**, 41 (1984).

[14] S. M. Walker, A. L. R. Thomas, and G. K. Taylor, Deformable wing kinematics in free-flying hoverflies, J. R. Soc. Interface **7**, 131 (2010).

[15] Y. P. Liu and M. Sun, Wing kinematics measurement and aerodynamics of hovering droneflies, J. Exp. Biol. **211**, 2014 (2008).

[16] J. H. Wu and M. Sun, Unsteady aerodynamic forces of a flapping wing, J. Exp. Biol. **207**, 1137 (2004).

[17] L. A. Miller and C. S. Peskin, When vortices stick: An aerodynamic transition in tiny insect flight, J. Exp. Biol. **207**, 3073 (2004).

[18] X. G. Meng and M. Sun, Aerodynamics and vortical structures in hovering fruitflies, Phys. Fluids **27**, 031901 (2015).

[19] X. Cheng and M. Sun, Very small insects use novel wing flapping and drag principle to generate the weight-supporting vertical force, J. Fluid Mech. **855**, 646 (2018).

[20] X. L. Mou, Y. P. Liu, and M. Sun, Wing motion measurement and aerodynamics of hovering true hoverflies, J. Exp. Biol. **214**, 2832 (2011).

[21] H. Aono, F. Liang, and H. Liu, Near- and far-field aerodynamics in insect hovering flight: An integrated computational study, J. Exp. Biol. **211**, 239 (2008).

[22] X. Cheng and M. Sun, Wing-kinematics measurement and aerodynamics in a small insect in hovering flight, Sci. Rep. **6**, 25706 (2016).

[23] S. E. Rogers, D. Kwak, and C. Kiris, Steady and unsteady solutions of the incompressible Navier-Stokes equations, AIAA J. **29**, 603 (1991).

[24] M. Sun and X. Yu, Aerodynamic force generation in hovering flight in a tiny insect, AIAA J. **44**, 1532 (2006).

[25] F. Manar and A. R. Jones, The effect of tip clearance on low Reynolds number rotating wings, AIAA Paper 2014-1452 (2014).

[26] J.-S. Han, J. W. Chang, and J.-H. Han, The advance ratio effect on the lift augmentations of an insect-like flapping wing in forward flight, J. Fluid Mech. **808**, 485 (2016).

[27] F. M. White, *Viscous Fluid Flow* (McGraw-Hill Higher Education, Boston, 1991), Vol. 2.

[28] See Supplemental Material at http://link.aps.org/supplemental/10.1103/PhysRevE.99.012419 for movies of the flying insects.

[29] G. R. Spedding and T. Maxworthy, The generation of circulation and lift in a rigid two-dimensional fling, J. Fluid Mech. **165**, 247 (1986).

[30] L. A. Miller and C. S. Peskin, A computational fluid dynamics of 'clap and fling' in the smallest insects, J. Exp. Biol. **208**, 195 (2005).

[31] N. Arora, A. Gupta, S. Sanghi, H. Aono, and W. Shyy, Lift-drag and flow structures associated with the "clap and fling" motion, Phys. Fluids **26**, 071906 (2014).

[32] J. C. Wu, Theory for aerodynamic force and moment in viscous flows, AIAA J. **19**, 432 (1981).

[33] H. J. Zhu and M. Sun, Unsteady aerodynamic force mechanisms of a hoverfly hovering with a short stroke-amplitude, Phys. Fluids **29**, 081901 (2017).